Journal of Geophysical Research: Solid Earth

RESEARCH ARTICLE
10.1029/2018JB015765

Absolute Stress Fields in the Source Region of the 1992 Landers Earthquake

Toshiko Terakawa[1] and **Egill Hauksson**[2]

[1]Earthquake and Volcano Research Center, Graduate School of Environmental Studies, Nagoya University, Nagoya, Japan, [2]Seismological Laboratory, Division of Geological and Planetary Sciences, California Institute of Technology, Pasadena, CA, USA

Key Points:
- Absolute stress tensors were obtained from earthquake focal mechanisms by combining the stress pattern with the Coulomb failure criterion
- A method to model 3-D absolute stress fields using focal mechanisms with a pore pressure parameter was developed
- The maximum shear stress in the source region of the Landers earthquake was estimated to be 44 ± 15 MPa at a depth of 5 km

Supporting Information:
- Supporting Information S1

Correspondence to:
T. Terakawa,
terakawa@seis.nagoya-u.ac.jp

Citation:
Terakawa, T., & Hauksson, E. (2018). Absolute stress fields in the source region of the 1992 Landers earthquake. *Journal of Geophysical Research: Solid Earth*, *123*, 8874–8890. https://doi.org/10.1029/2018JB015765

Received 13 MAR 2018
Accepted 22 SEP 2018
Accepted article online 29 SEP 2018
Published online 22 OCT 2018

Abstract Earthquake focal mechanisms are often inverted to obtain the deviatoric stress field. Because shear stress is equal to the frictional strength of the fault at the time of an earthquake, six components of the absolute stress tensor at the hypocenter can be obtained from a focal mechanism by combining deviatoric stress fields with the Coulomb failure criterion. For a data set of focal mechanisms determined for southern California earthquakes, including the 1992 Landers earthquake sequence, we calculated the absolute stress tensors at their hypocenters using a standard intrinsic friction coefficient under three pore pressure conditions, parameterized by the reference pore pressure at the optimally oriented faults to the stress field. Three absolute stress fields were obtained for southern California immediately before the Landers main shock by applying each data set of the stress tensors to an inversion scheme based on Bayesian statistical inference and Akaike's Bayesian Information Criterion. The coseismic stress field was calculated to obtain the absolute stress fields immediately after the main shock. The variations of the coseismic stress rotation were related to the reference pore pressure. Comparing this relation with that obtained through stress inversion, we determined the absolute stress field and the most plausible reference pore pressure to be hydrostatic. On average, the maximum shear stresses immediately before the main shock were 44 ± 15 and 79 ± 24 MPa at depths of 5 and 10 km, respectively. Earthquakes on the off-plate boundary faults in southern California occur on faults that are loaded by Anderson-Byerlee stress conditions.

1. Introduction

Earthquakes are a physical process that releases tectonic stresses in the Earth's crust by shear faulting, controlled by the Coulomb failure criterion. Knowledge regarding the frictional strength of faults and stress fields in the crust is absolutely necessary for understanding earthquake physics. In the 1970s, laboratory experiments showed that the friction coefficients of rocks are mostly constant within the range 0.6–1.0 under high fault-normal stresses ≥200 MPa (Byerlee, 1978). Worldwide in situ stress measurements for boreholes have universally indicated that the values measured in intraplate regions are in the same range as those obtained in laboratory experiments (Brudy et al., 1997; Zoback & Healy, 1992; Zoback & Townend, 2001). These results suggest that shear stresses on the fault would be in the range 50–100 MPa at seismogenic depths of 5–10 km assuming hydrostatic pore pressure conditions. However, the frictional strength of seismically active faults/plate boundaries and stress states in the crust remain unclear. This can be observed in the interdisciplinary debate on the strength of the San Andreas Fault (SAF) in California, which is called the *stress/heat flow paradox* (e.g., Brune et al., 1969; Lachenbruch & Sass, 1980; Rice, 1992; Scholz, 2000; Zoback et al., 1987). The long-standing debate stems from the technical and economic difficulties encountered when measuring stress in the crust and the frictional strength of faults in situ.

Stress for nonpolar materials is represented as a second-order symmetric tensor quantity with six independent parameters. Of them, the stress pattern or the deviatoric stress tensor normalized by the maximum shear stress, which constrains four of the six degrees of freedom, can be inferred from the focal mechanism/centroid moment tensor (CMT) solutions of seismicity through stress inversion analysis (e.g., Gephart & Forsyth, 1984; Hardebeck & Michael, 2006; Horiuchi et al., 1995; Michael, 1984, 1987; Rivera & Cisternas, 1990; Terakawa & Matsu'ura, 2008). The remaining two of the six degrees of freedom correspond to the maximum shear stress (the deviatoric stress magnitude) and to the isotropic part. The latter can be reasonably obtained by assuming that the vertical stress is the weight of the overburden. Therefore, it is essential to estimate the maximum shear stress in order to understand the absolute stress field.

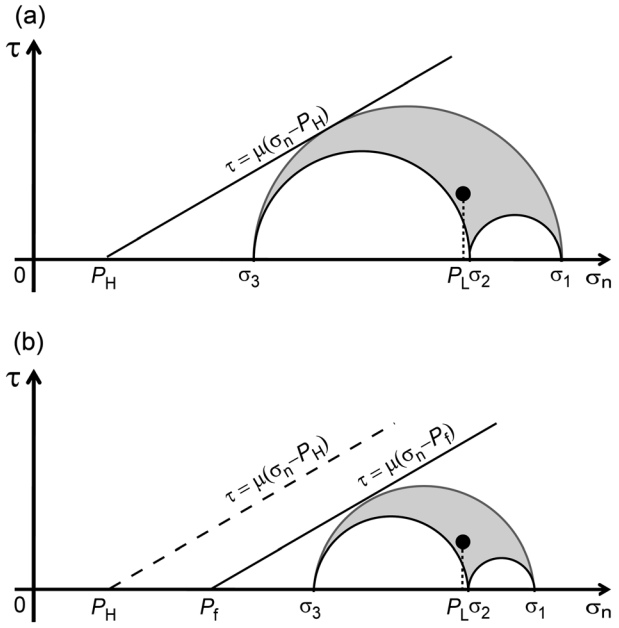

Figure 1. The maximum shear stress and the reference pore pressure P_f on a 3-D Mohr diagram. (a) The stress state under the hydrostatic pressure ($P_f = P_H$). (b) The stress state under overpressure ($P_f > P_H$). The horizontal and vertical axes show the normal and shear stresses, respectively (or frictional strength). σ_1, σ_2, and σ_3 are the maximum, intermediate, and minimum (compressive) principal stresses, respectively. P_H and P_L are the hydrostatic and lithostatic pressures, respectively. μ is the intrinsic friction coefficient of rocks. The black circles in a and b show the stress state on the horizontal plane, where the normal stress is equal to the weight of the overburden (= P_L).

At the time of the earthquake, shear stress equals the frictional strength of the fault and is described as follows:

$$\tau_s = \mu(\sigma_n - P_f), \quad (1)$$

where τ_s and σ_n are the frictional strength and normal stress (positive in compression) on a specified fault, respectively, P_f is pore pressure, and μ is the intrinsic friction coefficient of the rock. Terakawa et al. (2010, 2012) developed an inversion method to estimate 3-D pore pressure fields by mapping focal mechanism solutions of seismicity on a 3-D Mohr diagram for a given stress pattern. They assumed that the intrinsic friction coefficient was constant at 0.6 across the seismogenic depths. Using this method, six components of an absolute stress tensor at the hypocenter and at the origin time, as well as the pore pressure, were obtained by making the following two assumptions: (1) the vertical stress is the weight of the overburden and (2) optimally oriented faults relative to the stress pattern are critically stressed under hydrostatic pore pressure (Häring et al., 2008; Terakawa et al., 2010, 2012). The first assumption corresponds to the isotropic part of the absolute stress tensor, as previously described. For the second assumption, the Mohr-Coulomb failure line was set for optimally oriented faults under hydrostatic pressure, and the maximum shear stress was determined so that the largest Mohr circle came into contact with the Mohr-Coulomb failure line (Figure 1a). However, when more enhanced pore pressures at the optimally oriented faults are assumed, the maximum shear stress is estimated to be smaller (Figure 1b). This means that the pore pressure at the optimally oriented faults with a certain intrinsic friction coefficient controls the maximum shear stress.

In the present study, we calculated the six components of the absolute stress tensors using focal mechanism solutions derived for southern California earthquakes including the 1992 Landers earthquake (M_w 7.3), combining the stress pattern with the Coulomb failure criterion. For the criterion, we assumed three plausible pore pressure conditions with a fixed intrinsic friction coefficient with a standard value of 0.6. Using the three data sets of absolute stress tensors characterized by the pore pressure conditions, and based on Bayesian statistical inference and Akaike's Bayesian Information Criterion (ABIC; Akaike, 1977, 1980), we modeled the 3-D absolute stress field immediately prior to the Landers main shock. Using a well-studied rupture model (Wald & Heaton, 1994), we also calculated coseismic stress perturbations resulting from the main shock based on the elastic dislocation theory. We modeled the 3-D absolute stress field right after the main shock by superposing it to each absolute stress field characterized by the pore pressure conditions. When comparing the absolute stress fields before and after the main shock, a quantitative relationship was revealed between the coseismic stress rotation (temporal changes in the stress pattern) and the pore pressure condition. In addition, we evaluated the dependence of temporal changes in shear stress, acting on the main shock faults, on the reference pore pressure and those in the elastic strain energy due to the main shock, taking advantage of obtaining six components of the stress field. With a constraint on the coseismic stress rotation obtained through stress inversion and other comprehensive investigations on the results, we finally determined the most plausible pore pressure condition needed in order to estimate the 3-D absolute stress field in the source region of the large inland earthquake.

2. Development of a Method to Model 3-D Absolute Stress Fields From Earthquake Focal Mechanisms

Strike, dip, and rake values from earthquake focal mechanisms are inverted to determine the stress pattern, or the deviatoric stress tensor normalized by the maximum shear stress, which constrains four of the six degrees of freedom for an absolute stress tensor. Section 2.1 provides an explanation as to how the remaining two degrees of freedom at the hypocenter and at the reference time were determined by combining the

stress pattern with the Coulomb failure criterion characterized by a pore pressure parameter. In section 2.2 we outline the method used to model the 3-D absolute stress field from data sets of absolute stress tensors with a pore pressure parameter, based on Bayesian statistical inference and ABIC. In section 2.3 we explain how we evaluate the estimation errors of physical quantities in the absolute stress field.

2.1. Absolute Stress Tensors at Hypocenters and at the Reference Time

First we estimated the stress pattern from a data set of focal mechanism solutions using stress inversion (e.g., Gephart & Forsyth, 1984; Hardebeck & Michael, 2006; Horiuchi et al., 1995; Michael, 1984, 1987; Rivera & Cisternas, 1990; Terakawa & Matsu'ura, 2008). This process constrains four of the six degrees of freedom for an absolute stress tensor or the shape of the 3-D Mohr circles (Figure 1). For each event of the data set, we rationally assumed that the vertical stress at the hypocenter is equivalent to the weight of the overburden. This constrains another degree of freedom corresponding to the isotropic part of the absolute stress tensor or the absolute position of the 3-D Mohr circles on the horizontal axis of the Mohr diagram (P_L in Figure 1).

For the last degree of freedom, we assumed the Coulomb failure criterion in order to determine the maximum shear stress, which corresponds to the radius of the largest Mohr circle. Because earthquakes occur on preexisting faults, we may observe variation in focal mechanisms even in a uniform stress pattern (McKenzie, 1969). Based on results from the rock friction laboratory experiments and in situ stress measurements in boreholes, we fixed the intrinsic friction coefficient to be 0.6 (e.g., Byerlee, 1978; Brudy et al., 1997; Zoback & Healy, 1992; Zoback & Townend, 2001). We then attributed the variation in the focal mechanisms to that in the pore pressures (Terakawa et al., 2010, 2012). The 3-D Mohr diagram together with the Mohr-Coulomb failure line indicates that the pore pressure triggering events at optimally oriented faults relative to the stress pattern is the lowest in those triggering events at any preexisting faults at a certain depth. Using the pore pressure at the optimally oriented fault as a reference, and by examining the fault orientation relative to the stress pattern in the 3-D Mohr diagram, we can determine the increment in pore pressures (the excess pore pressures above the reference pore pressure) triggering events at any preexiting faults. Therefore, the reference pore pressure is the only parameter of the Coulomb failure criterion. With a given reference pore pressure, we can determine the maximum shear stress so that the Mohr-Coulomb failure line comes into contact with the largest Mohr circle. Note that we do not assume that all the events occur at the optimally oriented faults to the stress pattern but that an effective friction coefficient due to overpressurized fluids for each event depends on the fault orientation relative to the stress pattern and the reference pore pressure. The effects of dynamic slip weakening (e.g., Noda & Lapusta, 2010; Rice, 1992, 2006) and unusual minerals, which have low intrinsic friction coefficients (e.g., Lockner et al., 2011), can be also regarded as a decrease in the effective friction coefficient due to overpressurized fluids. With this procedure, we obtained six components of the absolute stress tensor at the hypocenter and at the origin time.

To obtain the absolute stress tensor at a reference time, t_r, we had to correct the absolute stress tensor at the origin time of each event, t_o. When the target event occurred before the reference time ($t_o < t_r$), we added the stress changes caused by all the events occurring at $t_o \le t < t_r$ to the absolute stress tensor at $t = t_o$. When the event occurred after the reference time ($t_o > t_r$), we subtracted the stress changes caused by all the events occurring at $t_r \le t < t_o$ from the absolute stress tensor at $t = t_o$. By varying the reference pore pressure, we were able to prepare the absolute stress tensor data sets at $t = t_r$ and model absolute stress fields by applying each dataset to the method described in the next section.

2.2. Modeling 3-D Absolute Stress Fields With the Reference Pore Pressure as a Selected Parameter

To model the 3-D absolute stress field at the reference time, we applied the inversion technique, based on Bayesian statistical inference and ABIC (e.g., Terakawa & Matsu'ura, 2008; Yabuki & Matsu'ura, 1992), to a data set of the absolute stress tensors at hypocenters. First, we represented each component of the absolute stress fields $\tau_{ij}(\mathbf{x})$ by superposing a finite number of tricubic B splines:

$$\tau_{ij}(\mathbf{x}) = \sum_{m=1}^{M} a_{ij}^{m} \Phi_m(\mathbf{x}), \tag{2}$$

where Φ_m are the tricubic B splines and a_{ij}^{m} $(m = 1, \cdots, M)$ are the expansion coefficients (the model parameters). The system of linear equations required to solve for the expansion coefficients was obtained from the absolute stress tensors data set $\boldsymbol{\tau}^n = \left[\tau_{ij}^n\right]$ $(n = 1, \cdots, N)$:

$$\tau_{ij}^{n} = \sum_{m=1}^{M} a_{ij}^{m} \Phi_m(\mathbf{x}_n) + e_{ij}^{n}, \tag{3}$$

where N is the number of absolute stress tensors and e_{ij}^{n} is the errors for the ij component of the nth tensors. Note that we removed the lithostatic pressure from the diagonal components of the absolute stress tensors of the data set in advance. Through this processing, we were able to estimate the absolute stress field in the region with no data to be close to lithostatic. These equations can be rewritten in a vector form as follows:

$$\mathbf{d} = \mathbf{F}\mathbf{a} + \mathbf{e}, \tag{4}$$

where $\mathbf{d}$ is a $6N \times 1$ data vector, $\mathbf{a}$ is a $6M \times 1$ model parameter vector, $\mathbf{F}$ is a $6N \times 6M$ coefficient matrix, and $\mathbf{e}$ is a $6N \times 1$ error vector. A stochastic model that relates $\mathbf{d}$ to $\mathbf{a}$ was obtained by assuming the errors to be Gaussian with a zero mean and a variance-covariance matrix, $\sigma^2\mathbf{E}$, denoted as follows:

$$p(\mathbf{d}|\mathbf{a};\ \sigma^2) = (2\pi\sigma^2)^{-6N/2} \|\mathbf{E}\|^{-\frac{1}{2}} \exp\left[-(\mathbf{d}-\mathbf{F}\mathbf{a})_{\mathrm{T}}\mathbf{E}^{-1}(\mathbf{d}-\mathbf{F}\mathbf{a})/2\sigma^2\right]. \tag{5}$$

Other than this system of linear equations, we can formulate the problem in the exactly same way as in Terakawa and Matsu'ura (2008). More specifically, we introduced a measure of roughness of the stress field, γ, to impose a prior constraint that the stress field must be spatially smooth to some degree from a physical viewpoint:

$$\gamma = \sum_{i=1}^{3}\sum_{j=1}^{3} \int_V \left(\frac{\partial \tau_{ij}}{\partial x_1}\right)^2 + \left(\frac{\partial \tau_{ij}}{\partial x_2}\right)^2 + \left(\frac{\partial \tau_{ij}}{\partial x_3}\right)^2 dV \ = \mathbf{a}^{\mathrm{T}}\mathbf{G}\mathbf{a}, \tag{6}$$

where $\mathbf{G}$ is a $6M \times 6M$ matrix and V is the whole study region. The prior constraint can be represented in a probability density function (PDF) with an unknown scale factor ρ^2 as follows:

$$p(\mathbf{a};\ \rho^2) = (2\pi\rho^2)^{-6M/2} \|\mathbf{G}\|^{1/2} \exp\left[-\frac{1}{2\rho^2}\mathbf{a}^{\mathrm{T}}\mathbf{G}\mathbf{a}\right]. \tag{7}$$

By incorporating the prior constraint (equation ((7)) with the stochastic model (equation (5)) using Bayes' rule and introducing the new hyperparameter $\alpha^2(=\sigma^2/\rho^2)$ instead of ρ^2, which denotes the relative weights of absolute stress tensor data to the prior constraint, a hierarchical, highly flexible model controlled by the hyperparameters σ^2 and α^2 was constructed as the posterior PDF:

$$p(\mathbf{a};\ \sigma^2,\ \alpha^2|\mathbf{d}) = c(2\pi\sigma^2)^{-(6N+6M)/2} \left\|\alpha^2\right\|^{\frac{6M}{2}} \|\mathbf{E}\|^{-\frac{1}{2}} \|\mathbf{G}\|^{\frac{1}{2}} \exp\left[-\frac{1}{2\sigma^2}s(\mathbf{a})\right] \tag{8}$$

with

$$s(\mathbf{a}) = (\mathbf{d}-\mathbf{F}\mathbf{a})^{\mathrm{T}}\mathbf{E}^{-1}(\mathbf{d}-\mathbf{F}\mathbf{a}) + \alpha^2\mathbf{a}^{\mathrm{T}}\mathbf{G}\mathbf{a}, \tag{9}$$

where c is a normalizing factor independent of the model parameter $\mathbf{a}$.

For fixed values of the hyperparameters σ^2 and α^2, the model parameters, $\mathbf{a}^*$, that maximize posterior PDF and the variance-covariance matrix $\mathbf{C}(\mathbf{a}^*)$ were obtained as follows (Jackson & Matsuura, 1985):

$$\mathbf{a}^* = \left(\mathbf{F}^{\mathrm{T}}\mathbf{E}^{-1}\mathbf{F} + \alpha^2\mathbf{G}\right)^{-1}\mathbf{F}^{\mathrm{T}}\mathbf{E}^{-1}\mathbf{d}, \tag{10}$$

$$\mathbf{C}(\mathbf{a}^*) = \sigma^2\left(\mathbf{F}^{\mathrm{T}}\mathbf{E}^{-1}\mathbf{F} + \alpha^2\mathbf{G}\right)^{-1}. \tag{11}$$

To select the best model characterized by the hyperparameter α^2, we iteratively calculated ABICs to search for the value of $\widehat{\alpha}^2$, which minimizes ABIC:

$$\mathrm{ABIC} = 6N\log s(\mathbf{a}^*) - 6M\log\alpha^2 + \log\left\|\mathbf{F}^{\mathrm{T}}\mathbf{E}^{-1}\mathbf{F} + \alpha^2\mathbf{G}\right\| + C', \tag{12}$$

where C' is a constant, which is independent of α^2. A necessary condition for the minimum of ABIC derives

$$\sigma^2 = \frac{s(\mathbf{a}^*)}{6N}. \tag{13}$$

The best estimate of the model parameters, $\widehat{\mathbf{a}}$, the hyperparameter, $\widehat{\sigma}^2$, and the variance-covariance matrix $\mathbf{C}(\widehat{\mathbf{a}})$ were obtained by substituting $\widehat{\alpha}^2$ into equation (10), $\widehat{\mathbf{a}}$ into equation (13), $\widehat{\alpha}^2$ and $\widehat{\sigma}^2$ into equation (11). Finally,

each component of the absolute stress field was obtained by substituting $\hat{\mathbf{a}}$ into equation (2). By using this method, the absolute stress field was modeled using only the reference pore pressure parameter. We need not consider the loading processes in the crust.

2.3. The Estimation Errors of the Stress Tensor

When a physical quantity, Q, is represented by the linear combination of the model parameters, (equation (14)), the variance of the quantity from the variance-covariance matrix $\mathbf{C}(\hat{\mathbf{a}})$ can be calculated as follows:

$$Q = \sum_{i=1}^{6M} q_i a_i, \tag{14}$$

$$\mathrm{var}(Q) = {}^{\mathrm{T}}\mathbf{q}\mathbf{C}(\hat{\mathbf{a}})\mathbf{q}, \tag{15}$$

where q is the $6M \times 1$ vector where its ith component is q_i. For example, one can calculate the variance of each component of the absolute stress field using equation (15) and evaluate the estimation errors using, for example, the square root of the variance (the standard deviation). However, it is not that straightforward to evaluate the variance of physical quantities like the maximum shear stress, because they are not represented by the linear combination of the model parameters. The best estimates of the model parameters, $\hat{\mathbf{a}}$, and the variance-covariance matrix, $\mathbf{C}(\hat{\mathbf{a}})$, mean that the probability distribution of the model parameters is as follows:

$$p(\mathbf{a}) = (2\pi)^{-n/2} \|\mathbf{C}(\hat{\mathbf{a}})\|^{-\frac{1}{2}} \exp\left[-\frac{1}{2}{}^{\mathrm{T}}(\mathbf{a}-\hat{\mathbf{a}})\mathbf{C}(\hat{\mathbf{a}})^{-1}(\mathbf{a}-\hat{\mathbf{a}})\right]. \tag{16}$$

To evaluate the estimation errors of scalar quantities in general, a set of multivariate normal random numbers was generated following equation (16), which is a set of the synthetic model parameters. The absolute stress tensor and the focused scalar quantity were then calculated. This process was repeated again and again, and the confidence region of the quantity was evaluated.

3. The 3-D Absolute Stress Field in the Source Region of the 1992 Landers Earthquake

Large earthquakes significantly influence tectonic stress fields in the broader region surrounding their source area. To constrain the absolute stress field near the source region, and as the coseismic stress perturbation caused by large earthquakes can be estimated, it is crucial to determine how the earthquake alters the tectonic stress patterns, which is known as the coseismic stress rotation (e.g., Hardebeck & Hauksson, 2001; Hasegawa et al., 2011; Wesson & Boyd, 2007). The M_w 7.3 Landers earthquake occurred on 28 June 1992 at the southern end of the eastern California shear zone in the United States, within 20–30 km north of the southern SAF (Figure 2). This is the largest main shock-aftershock sequence recorded by the Southern California Seismographic Network since monitoring began in the 1920s (Hauksson et al., 1993). Recently, the catalog of focal mechanism solutions for seismicity in southern California was significantly improved by including both *S*/*P* amplitude ratios and first motion polarities (Yang et al., 2012).

The aim of this study was to use the large data set of focal mechanism solutions to model the absolute stress field near the source region of the Landers earthquake according to the method outlined in section 2. For this purpose we estimated the stress patterns for the preperiod and postperiod of the Landers earthquake using an inversion method of CMT data (Terakawa & Matsu'ura, 2008; section 3.1). Combining the stress pattern with the Coulomb failure criterion parameterized by the reference pore pressures, we modeled the 3-D absolute stress fields immediately before the main shock (section 3.2). The coseismic stress field caused by the main shock was then calculated (section 3.3) and was added to each absolute stress field obtained in section 3.2, in order to model the 3-D absolute stress fields immediately after the main shock. Comparing the absolute stress fields before and after the main shock directly, the quantitative relationship between the coseismic stress rotation and the reference pore pressure was determined. This relationship was then compared with the coseismic stress rotation obtained by stress inversion in section 3.1, which constrains the most appropriate reference pore pressure needed to estimate the 3-D absolute stress fields. Taking advantage of obtaining six components of the stress field, we also evaluated the dependence of temporal changes in shear stress, acting on the main shock faults, on the reference pore pressure and those in the

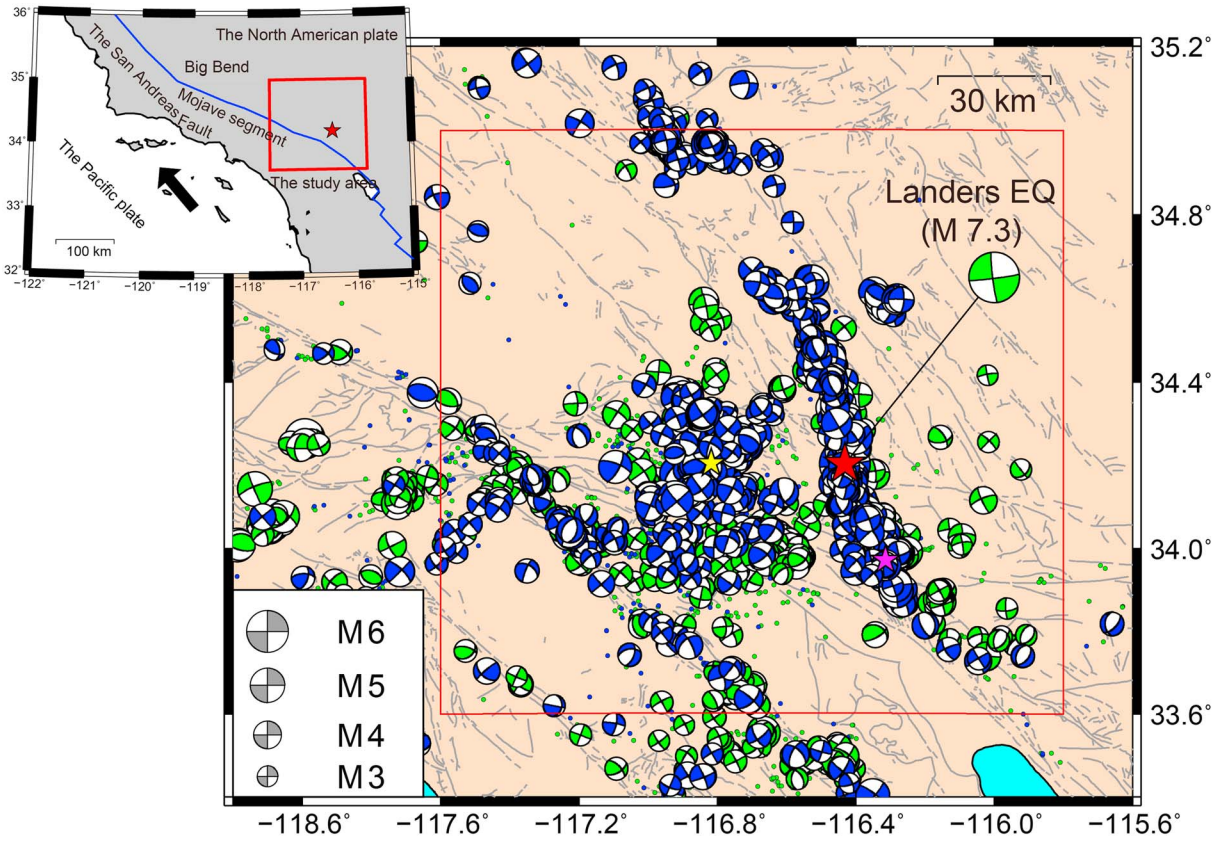

Figure 2. Map of the study area and data for the analysis (period: 1 January 1981 to 15 October 1999). The hypocenters of the 1992 Landers (M_w 7.3), the 1992 Joshua Tree (M_w 6.1), and the 1992 Big Bear (M_w 6.5) earthquakes are indicated by red, pink, and yellow stars, respectively. Focal mechanism solutions with $M \geq 3$ are represented by the lower hemisphere projection of focal spheres. The data for the preperiod and postperiod of the Landers earthquake are shown in green and blue, respectively (Yang et al., 2012). The green and blue circles denote events with $2 \leq M < 3$ for the preperiod and postperiod of the Landers earthquake, respectively. Major Late Quaternary faults are indicated by gray lines (Jennings, 1994). The location and the tectonic setting of the study area are shown in the inset figure. The blue line in the figure shows the San Andreas Fault (SAF; Bird, 2003). The black arrow shows the relative direction of the plate motion of the Pacific plate to the North American Plate.

elastic strain energy caused by the main shock. Based on this comprehensive consideration, we finally determined the absolute stress field immediately before the Landers earthquake (the background stress field).

3.1. Stress Patterns for the Preperiod and Postperiod of the Landers Earthquake

The region surrounding the source region of the 1992 Landers earthquake (longitude: 115.8°W–117.6°W, latitude: 33.6°N–35.0°N, depth: 0–15 km) was targeted as the study region to estimate the stress pattern and the coseismic stress rotation using the CMT data inversion method (Terakawa & Matsu'ura, 2008). The original data set consisted of 6,275 focal mechanism solutions for seismicity with high qualities (ranks of A and B) in the target region obtained during the period from 1 January 1981 to 15 October 1999 in the catalog by Yang et al. (2012). We used focal mechanism solutions with $M \geq 2$ as an unbiased data set for stress inversion (Figure 2). The focal mechanism solutions were converted to CMT data according to the well-known relation between moment magnitude and seismic moment (Hanks & Kanamori, 1979). We divided the data into two groups for which the number of data was 2,135 and 3,373 for the Landers earthquake preperiod (1 January 1981 to 28 June 1992) and the postperiod (28 June 1992 to 15 October 1999), respectively. The method was then applied to each data set.

To discretize the stress field, we distributed 3,078 ($19 \times 18 \times 9$) tricubic B splines (basis functions) with equal spacing of 10- and 2.5-km grid intervals in the horizontal and vertical directions, respectively. To estimate the spatial variation in the stress pattern near the faults of the Landers earthquake (the main shock faults) with

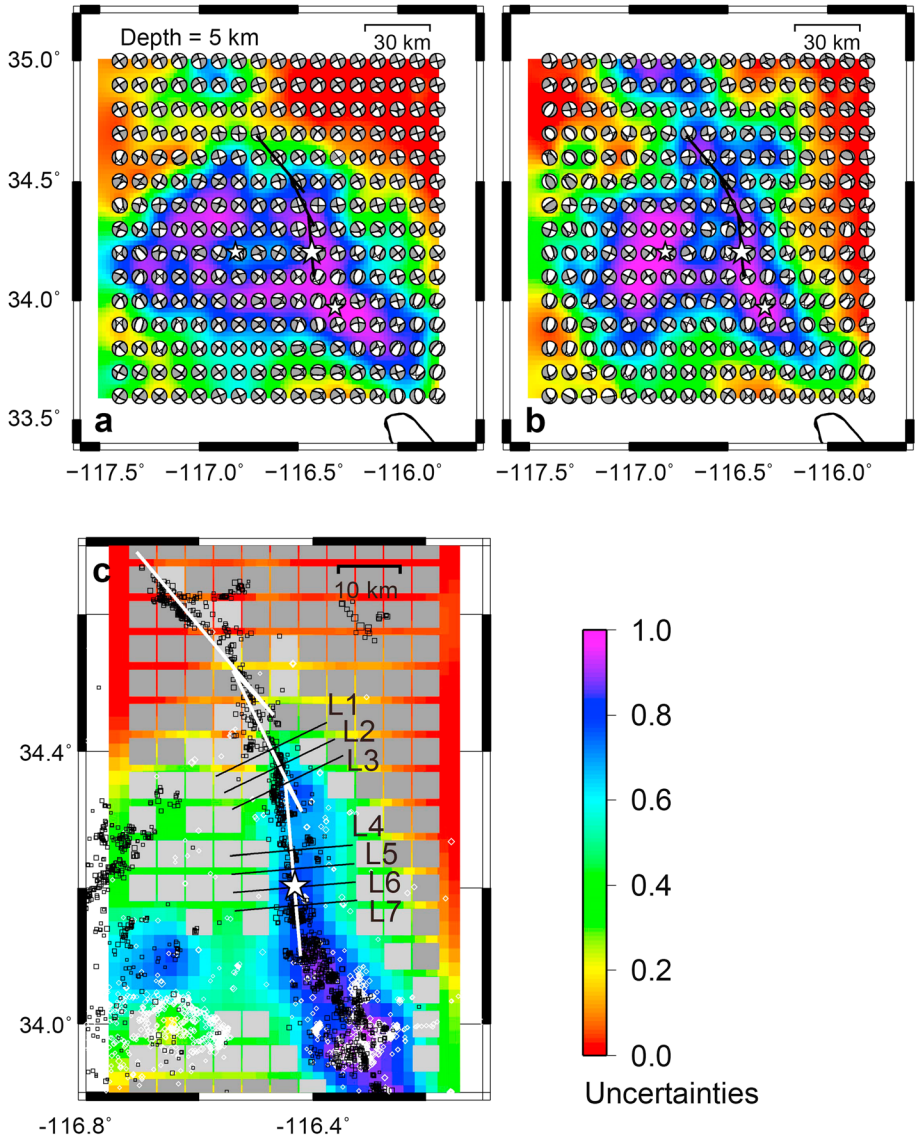

Figure 3. The tectonic stress pattern for the preperiod and postperiod of the Landers earthquake (depth = 5 km). (a) The tectonic stress pattern for the preperiod. (b) The tectonic stress pattern for the postperiod. The stress pattern is represented with the lower hemisphere projection of focal spheres, where nodal planes correspond to the maximum shear planes at each location. The color scales in (a) and (b) show the uncertainties of the stress pattern, which are measured with the average inner tensor product (ITP) between the best stress tensor and acceptable ones (Terakawa, 2017). The big and small stars denote the Landers, the Joshua tree, and the big bear earthquakes. The three black segments denote the main shock faults of the Landers earthquake used in the analysis (Wald & Heaton, 1994). (c) The coseismic stress rotation due to the Landers earthquake. The closeness of the two stress tensors for the preperiod and the postperiod of the main shock was measured using the ITP between them. The results with large uncertainties are masked by the gray squares. The dark and light gray squares indicate the standard deviations of ITPs with ≥0.4 and with 0.3–0.4, respectively.

higher resolution, we distributed 2,691 (23 × 13 × 9) tricubic B splines with equal spacing for a smaller horizontal local support (5 km) in the vicinity of the main shock faults (longitude: 116.2°W–116.7°W, latitude: 33.85°N–34.75°N, depth: 0–15 km).

For each period the best estimates of the model parameters and the variance covariance matrix were obtained for the stress field. These take the same forms as those presented in equations (10) and (11). Using the best estimates of the model parameters, each component of the stress field for the two time periods was obtained and denoted as a continuous function, although only the relative values of the six components have physical meaning. Figures 3a and 3b show the stress pattern with the lower hemisphere

projection of the focal spheres, where nodal planes correspond to the maximum shear planes at each location. For both the periods, the stress pattern was roughly characterized by strike-slip faulting with the maximum compressive principal stress axes trending in a northeast-southwest to north-south direction (Figures 3a and 3b). This remarkable feature was consistent with the results found in Yang and Hauksson (2013). To examine the uncertainty of the stress pattern for each period, 100 sets of the synthetic model parameters were generated according to equation (16), and the inner tensor product (ITP) of the stress tensor was calculated using both the best estimates of the model parameters (the best stress pattern) and the synthetic model parameters (the possible stress pattern; Michael, 1987):

$$\mathrm{ITP} = \frac{\sum_{i=1}^{3}\sum_{j=1}^{3} s_{ij}^{\mathrm{best}} s_{ij}^{\mathrm{syn}}}{\sqrt{\sum_{i=1}^{3}\sum_{j=1}^{3}\left(s_{ij}^{\mathrm{best}}\right)^2}\sqrt{\sum_{i=1}^{3}\sum_{j=1}^{3}\left(s_{ij}^{\mathrm{syn}}\right)^2}} \tag{17}$$

where s_{ij}^{best} and s_{ij}^{syn} are components of the best stress pattern and the possible stress pattern, respectively. The quantity ITP ranges from -1 to $+1$, where $+1$ indicates that the two (normalized) stress tensors are exactly the same and -1 indicates that they are exactly opposite. The ITP values were examined, and the average value was evaluated as a measure of the uncertainty of the stress pattern (Terakawa, 2017). The confidence interval of the uncertainty of the stress pattern was also evaluated. A stress pattern with larger average ITP denotes more reliability in the estimates (Figures 3a and 3b).

In order to measure the confidence interval of the coseismic stress rotation, 100 sets of synthetic model parameters for each period were generated, and the stress tensors used to evaluate the ITP for the preperiod and the postperiod were calculated. The average and standard deviation of the ITPs were evaluated as measures of the coseismic stress rotation and its 68% confidence interval, respectively. The reliable results of the average ITP values with associated uncertainties (the standard deviations of ITPs) smaller than 0.3 are shown in Figure 3c. The results of the coseismic stress rotation were more reliable in the region where more sufficient data were available for both the periods (Figure 3c). Further, the results were most robust around the southern half of the central segment and the southern segment of the main shock faults where the ITP values were greater than 0.7. ITP values of 0.6, 0.8, and 0.9 noted in the reliable region corresponded roughly to angles of rotation of the maximum compressive principal stress axis of 30°, 23°, and 13°, respectively (Figure S1).

3.2. Modeling 3-D Absolute Stress Fields With Three Representative Reference Pore Pressures

In this section, we prepared data sets of absolute stress tensors at the origin time of the Landers earthquake (the reference time) using the procedure described in section 2.1. We used all the focal mechanism solutions for the preperiod of the main shock in the original data set (section 3.1), and the number of data values was 2,464. First, the absolute stress tensors at the origin time of events were calculated by combining the stress pattern for the preperiod obtained in section 3.1 (Figure 3a) with the Coulomb failure criterion (with the intrinsic friction coefficient of 0.6). In this calculation, we introduced an overpressure coefficient, C, to measure the reference pore pressures, P_f, as follows:

$$C = \frac{P_r - P_H}{P_L - P_H}, \tag{18}$$

where P_H and P_L are the hydrostatic and lithostatic pressures, respectively. Assuming a rock density of 3,000 kg/m^3, three data sets of absolute stress tensors at the hypocenters and at the origin times were created with reference pore pressures of C = 0.0, 0.5, and 0.8, respectively.

Corrections of the absolute stress tensors for the preperiod events were simply made by subtracting only the stress drop tensors themselves from absolute stress tensors at the origin times. The stress drops of events with an $M \geq 2$ in the Landers region were relatively constant at 5–10 MPa, although scatter was observed in those of smaller events (Trugman & Shearer, 2017). Therefore, we assumed the magnitude of the stress drop tensors to be 5 MPa.

To discretize the absolute stress field, we used the same tricubic B splines as those in the previous section. Applying the procedure described in section 2.2 to the three data sets of absolute stress tensor at the

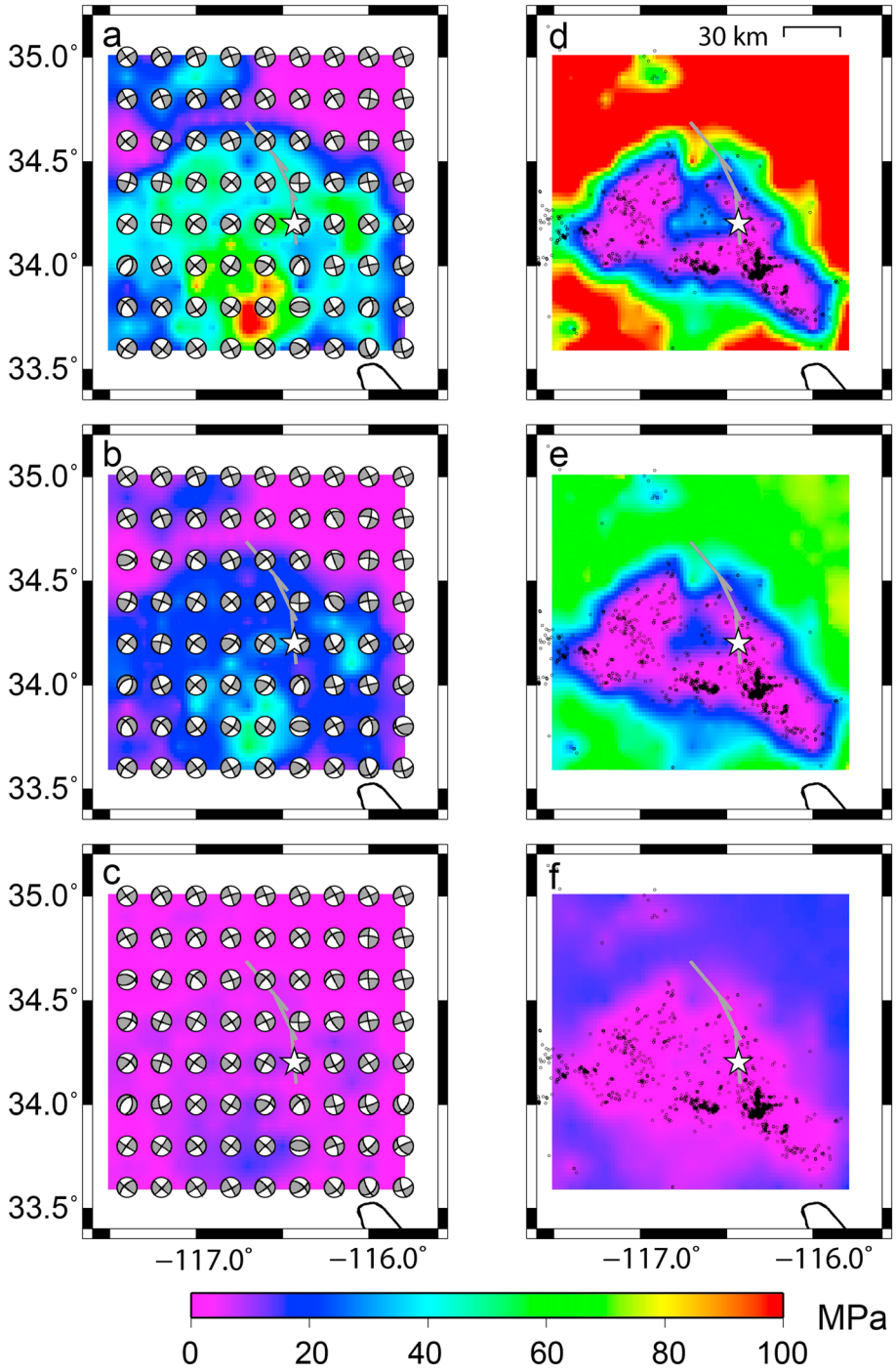

Figure 4. The absolute stress field at a depth of 5 km immediately before the Landers earthquake. The absolute stress fields calculated with (a) $C = 0.0$, (b) $C = 0.5$, and (c) $C = 0.8$. The color scales in (a)–(c) show the maximum shear stress. The stress pattern is shown in the same way as in Figure 3. The uncertainties (68% confidence intervals) of the estimates of the maximum shear stress calculated f with (d) $C = 0.0$, (e) $C = 0.5$, and (f) $C = 0.8$. The black dots denote the hypocenters of events (depth: 0–10 km) used in the analysis. The star is same as that in Figure 3. The gray segments denote the main shock faults of the Landers earthquake used in the analysis.

reference time, we obtained the 3-D absolute stress fields (immediately before the Landers earthquake) with $C = 0.0$, 0.5, and 0.8 (Figure 4). Because only few events occurred around the northernmost segment of the main shock faults, the estimation errors there were large. On average, the resulting

Table 1
Structural Parameters Used for Calculating the Coseismic Stress Perturbations Due To the Landers Earthquake

	Thickness (km)	ρ (kg/m^3)	λ (GPa)	μ (GPa)
Lithosphere	30	3,000	40	40
Asthenosphere	∞	3,400	90	60

maximum shear stresses (the deviatoric stress magnitudes) within 10 km of the central and southern segments of the main shock faults and at a depth of 5 km were 44 ± 15, 20 ± 8.1, and 5.4 ± 2.5 MPa for reference pore pressures of C = 0.0, 0.5, and 0.8, respectively. The estimation errors indicate a 68% confidence interval. Those at a depth of 10 km were, on average, 79 ± 24, 38 ± 13, and 11 ± 2.8 MPa (Figure S2).

3.3. Estimating the 3-D Absolute Stress Field

To investigate the dependence of coseismic stress rotation on the reference pore pressure, we calculated the coseismic stress perturbations caused by the Landers earthquake using the analytical slip response function (Fukahata & Matsu'ura, 2005, 2006) together with the source rupture model estimated by Wald and Heaton (1994) and the elastic parameters presented in Table 1 (Figures 5 and S3 in the supporting information). The coseismic stress field was superposed on the absolute stress fields immediately before the Landers earthquake, and then the absolute stress fields after the main shock were obtained with C = 0.0, 0.5, and 0.8. The maximum shear stress in each absolute stress field immediately before the main shock was relatively uniform in the horizontal plane, regardless of the distance from the main shock faults (Figure 4). In contrast, those of the coseismic stress perturbation decreased with distance from the main shock faults, where values averaged along the rupture segments were 18, 11, 8, 5, 4, 3, and 2 MPa at 0.5, 1, 2, 4, 6, 8, and 10 km from the main shock faults (Figure 5). The coseismic stress rotation across the main shock faults was examined by comparing the absolute stress fields before and after the main shock directly with ITP (Figure 6). The coseismic stress rotations along the seven profiles across the main shock faults with ITPs $\leq$ 0.9 were localized within 1, 2, and 4 km from the main shock faults in the results where C = 0.0, 0.5, and 0.8, respectively (Figure 6). The widths of the coseismic stress rotation across the main shock faults were compared with those obtained by stress inversion as outlined in section 3.1 (Figures 3c and 6). The observed results were most closely aligned with the stress field under hydrostatic reference pore pressure where C = 0.0 (Figure 6a).

Changes in the magnitude and the direction of shear stresses acting on the main shock faults caused by the main shock were further investigated (Figure 7). Changes in the direction of shear stresses were examined by calculating the inner product of the resolved shear traction vectors for the preperiod and the postperiod of the main shock. The diamonds in Figure 7 represent locations with negative inner product values, indicating that the direction of the resolved shear tractions reversed after the main shock. In the results with C = 0.0,

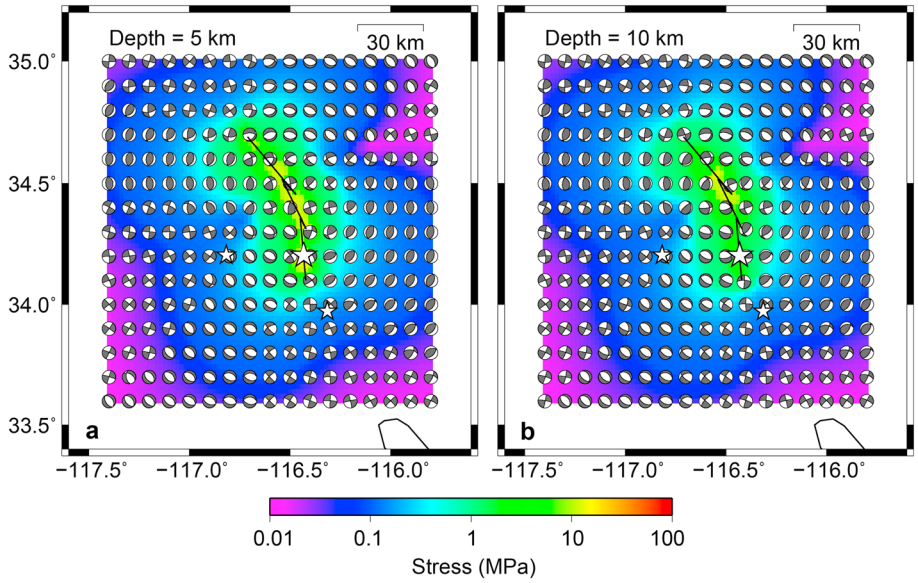

Figure 5. Coseismic stress perturbation due to the Landers earthquake at depths of (a) 5 km and (b) 10 km. The coseismic stress perturbation pattern is shown in the same way as that in Figure 3. The color scales in (a) and (b) denote the maximum shear stresses of the coseismic stress perturbation. The stars and black segments are identical to those in Figure 3.

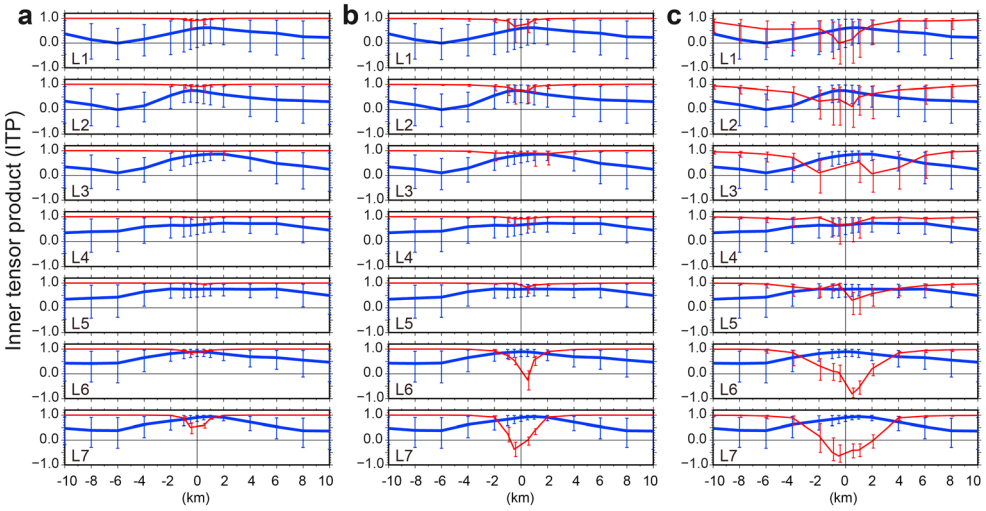

Figure 6. Comparison of the coseismic stress rotation with various reference pore pressure to that obtained through stress inversion. The seven profiles of the coseismic stress rotations along L1–L7 (Figure 3c) in the results with (a) $C = 0.0$, (b) $C = 0.5$, and (c) $C = 0.8$. The coseismic stress rotation directly derived from absolute stress fields and that obtained through the stress inversion are indicated by red and blue lines, respectively. The vertical lines denote the 95% confidence interval.

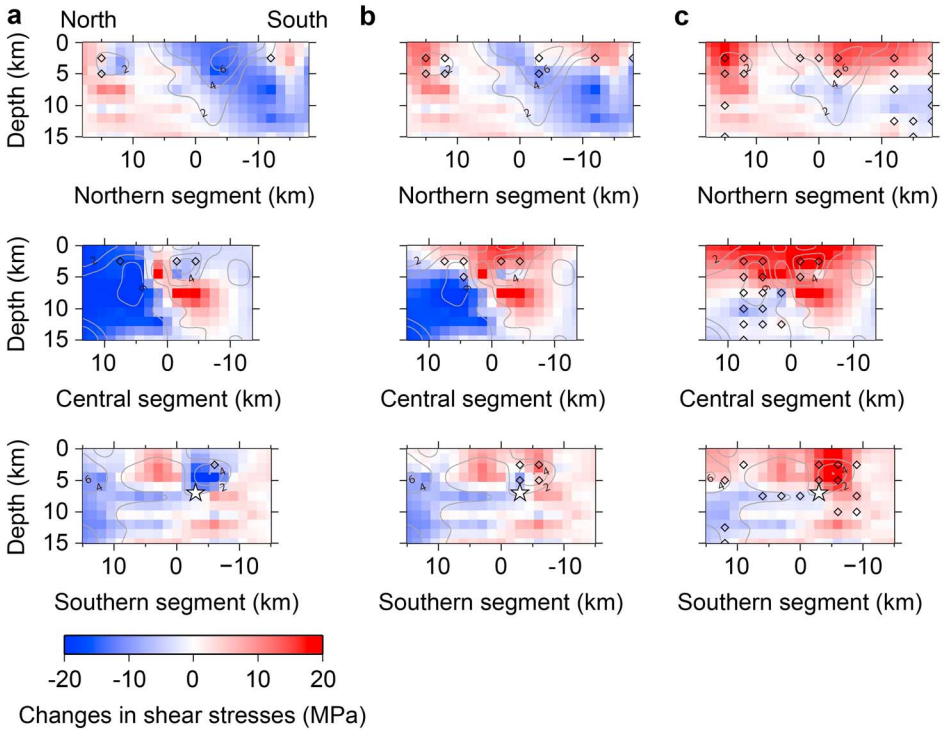

Figure 7. Changes in shear stresses on the main shock faults due to the Landers earthquake. (a) $C = 0.0$, (b) $C = 0.5$, and (c) $C = 0.8$. The color scales show the changes in magnitude of the shear stresses acting on the three segments. The negative and positive values mean that the shear stress decreased and increased, respectively, after the Landers earthquake. The diamonds indicate the locations where the direction of shear stress reversed following the Landers event. The gray contour lines (at 2-m intervals) show the slip distribution estimated by Wald and Heaton (1994; Figure S3a). The star shows the hypocenter of the Landers earthquake (Wald & Heaton, 1994).

shear stresses decreased after the main shock, although they increased at both the ends of the rupture zone (Figure 7a). The direction of resolved shear tractions did not change remarkably, indicating that shear stresses were basically released by the main shock (Figure 7a). Similar tendencies were observed in the results with C = 0.5; however, the area where shear stresses were released shrunk (Figure 7b). On the other hand, in the results with C = 0.8, the shear stresses overshot and increased on most areas of the main shock faults. Given that earthquakes occur to release tectonic stresses accumulated within the crust, this seems unrealistic.

Temporal changes in the elastic strain energy within 10 km from the main shock faults were roughly evaluated, as six components of the absolute stress tensors were obtained in this study (Figure S4). In the rough estimates, temporal changes in the elastic strain energy caused by the main shock were -7.8×10^{16}, -3.0×10^{16}, and $+5.6 \times 10^{14}$ Nm in the results with C = 0.0, 0.5, and 0.8, respectively. In the results with C = 0.8, the elastic strain energy increased after the main shock. This seems unrealistic. The elastic strain energy released by the main shock is theoretically consumed in the form of radiation, friction, and fracture surface energies. This indicates that the released elastic strain energy must be larger than at least the radiation energy, which is estimated to be about 4.3×10^{16} Nm (Kanamori et al., 1993). In this regard, the absolute stress field with C = 0.0 appears to be the most realistic, and that with C = 0.5 cannot be rejected within uncertainties.

Based on the results of the coseismic stress rotation, changes in the shear stress acting on the main shock faults, and those in the elastic strain energy, we comprehensively conclude that the stress field with C = 0.0 is the most realistic. This indicates that off-plate boundary active faults in southern California are under the Anderson-Byerlee state of stress (Anderson, 1951; Byerlee, 1978). On average, the maximum shear stresses immediately before the Landers earthquake (around the central and southern segments of the main shock faults) were 44 ± 15 and 79 ± 24 MPa at depths of 5 and 10 km, respectively (Figures 4a, 4d, S2a, and S2d). Those within 1 km from the main shock faults were 44 ± 13 and 81 ± 22 MPa at depths of 5 and 10 km, respectively (Figure 8), indicating that the maximum shear stress was slightly enhanced near the main shock fault segments.

4. Discussion

In the method used to model the 3-D absolute stress field in section 2, we did not explicitly incorporate the quasi-static momentum equation. Instead, we imposed a prior constraint that the stress field must be spatially smooth to some degree from a physical perspective (equation (6)). We also considered imposing another prior constraint that the quasi-static momentum equation must be satisfied, which substitutes for the original prior constraint on the smoothness of the stress field, by introducing another measure of roughness of the stress field γ':

$$\gamma' = \sum_{i=1}^{3} \int_V \left(\frac{\partial \tau_{i1}}{\partial x_1} + \frac{\partial \tau_{i2}}{\partial x_2} + \frac{\partial \tau_{i3}}{\partial x_3} \right)^2 dV = \mathbf{a}^{\mathrm{T}} \mathbf{G}_2 \mathbf{a}. \tag{19}$$

Using the formula that uses $\mathbf{G}_2$ instead of $\mathbf{G}$ in equations (10) and (11), we obtained the 3-D absolute stress fields (Figure S5). The difference in the prior constraint did not result in significantly different absolute stress fields in the region within small uncertainties (Figures 4 and S5). The coseismic stress rotation expected from the absolute stress field was not affected by the prior constraint, either (Figures 6a and S6). To confirm whether the prior constraints were appropriate, we computed apparent static body force $\mathbf{f} = (f_i)$ from the absolute stress tensor $\boldsymbol{\tau} = [\tau_{ij}]$:

$$f_i = -\sum_{j=1}^{3} \frac{\partial \tau_{ij}}{\partial x_j}. \tag{20}$$

We compared the magnitudes of the apparent body force in the absolute stress field with C = 0.0, where they are the most significant among the three absolute stress fields with C = 0.0, 0.5, and 0.8 (Figure S7). The apparent body force with the original prior constraint (equation (6)) was nearly double as that obtained with the prior constraint on the quasi-static momentum equation, but it was less than 0.1% of the gravitational force. This indicates that the original prior constraint was appropriate enough to model realistic stress fields from focal mechanism solutions.

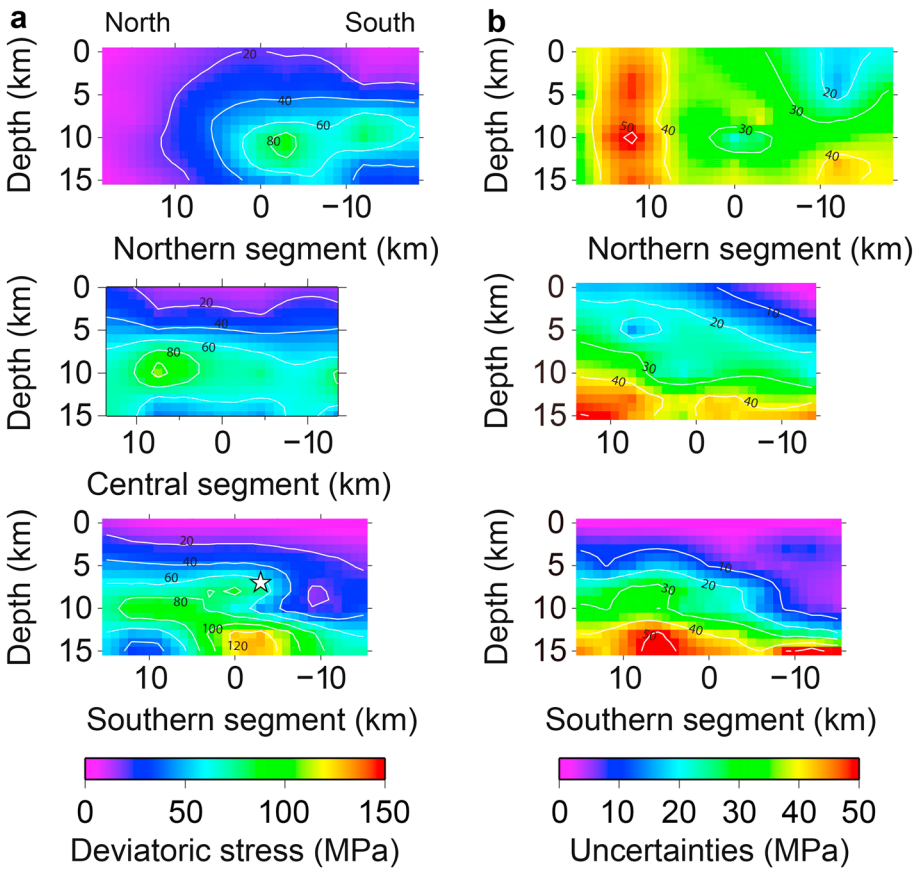

Figure 8. The maximum shear stress acting on the main shock faults of the Landers earthquake. (a) The maximum shear stress of the absolute stress field with the most plausible pore pressure coefficient, $C = 0.0$. The white lines indicate the contour lines at 20-MPa interval. The star denotes the hypocenter of the main shock. (b) The 68% confidence region of the maximum shear stress. The white lines indicate the contour lines at 10-MPa interval.

The friction coefficient and the frictional strength of the source fault of the 1995 Kobe (Hyogo-ken Nanbu) earthquake (at depths of 0.3–1.5 km) were estimated with a similar approach to the present study. Yamashita et al. (2004) reconstructed the shear stress on the fault immediately before the Kobe earthquake by subtracting the coseismic stress perturbation from in situ stress measurements of the hydraulic fracturing experiment conducted after the event. The gradient of differential stress, which is twice that of the maximum shear stress, was estimated to be 19 MPa/km with a hydrostatic pore pressure and a friction coefficient of 0.6. The maximum shear stress extrapolated to a depth of 5 km is 48 MPa, which is consistent with the results for the Landers source region (44 ± 15 MPa) obtained in the present study.

Fluid diffusion is one of the important mechanisms that can trigger aftershocks following the Landers earthquake (Bosl & Nur, 2002). This suggests that decreases in frictional strength could be an important mechanism for triggering aftershocks at faults unfavorably oriented relative to the tectonic stress pattern (Sibson, 1992; Terakawa, 2014; Terakawa et al., 2010, 2012). When a data set is biased by these events at unfavorably oriented faults, stress inversion tends to attribute statistical changes in focal mechanism solutions to the coseismic stress rotation caused by the main shock (Terakawa et al., 2013). When considering the decrease in frictional strength resulting from the fluid diffusion process, the coseismic stress rotation obtained in section 3.1 (Figures 3 and 6) can be somewhat overestimated. Therefore, the maximum shear stress constrained from the coseismic stress rotation might represent the lower limit of stress.

When the absolute stress tensors were calculated by combining the stress pattern with the Coulomb failure criterion, it was assumed that pore fluid pressures were, in the least, hydrostatic. The absolute stress field obtained with the most plausible reference pore pressure, $C = 0.0$ (Figure 5a), was consistent with the Anderson-Byerlee condition (Anderson, 1951; Byerlee, 1978) and with the results of in situ stress

measurements (Brudy et al., 1997; Zoback & Townend, 2001; Zoback & Healy, 1992). Nevertheless, if a dry condition was assumed (where the reference pore pressure would be 0 MPa), the maximum shear stress would be larger by a factor of 1.6, and the stress values in southern California would be estimated to be 70 and 126 MPa at depths of 5 and 10 km, respectively. In this case, it would be expected that the width of the coseismic stress rotation would be <1 km and still be within the 95% confidence interval of the inverted stress pattern presented in section 3.1 (Figure 6). Hence, the estimate of the maximum shear stress obtained in this study might also represent the lower limit.

Some previous studies proposed methods to model 3-D absolute stress fields in the crust and estimated the absolute stress field in southern California (Bird, 2017; Luttrell & Smith-Konter, 2017). Bird (2017) divided the absolute stress field into topographic and tectonic stress fields other than lithostatic pressures. The modeling is based on the equation of quasi-static stress equilibrium for each stress field, with the following two kinds of constraints: the stress pattern in the database of the World Stress Map (Heidbach et al., 2008) and deviatoric stresses from dynamic model simulations of lithospheric deformation computed with the finite element code. The deviatoric stress magnitude (the maximum shear stress) peaks at 120–150 MPa around the depth of 5 km. The value is 3 to 4 times as large as that of the present study. The value seems to be mainly governed by the assumed effective friction coefficient in the unfaulted region (0.85). If the effective friction coefficient in the unfaulted region is assumed to be 0.4, which corresponds to the standard friction coefficient (0.6) under hydrostatic pressure ($C = 0.0$), the deviatoric stress magnitude would be roughly 56–70 MPa, which is consistent with the results of the present study.

On the other hand, Luttrell and Smith-Konter (2017) also divided the absolute stress field into topographic and tectonic stress fields and determined the former field according to the methods of Luttrell et al. (2011) and Luttrell and Sandwell (2012). They assumed that the tectonic stress fields are more dominant than the topographic ones over the targeted active tectonic region. They, further, estimated the absolute stress fields that explain the inverted stress pattern observed by Yang and Hauksson (2013) in the least squares sense despite perturbation from the topographic stress fields. As pointed out in Luttrell and Smith-Konter (2017), and as demonstrated in Figure 4, the maximum shear stress (the deviatoric stress magnitude) cannot generally be determined only from the stress pattern. Therefore, Luttrell and Smith-Konter (2017) estimated the lower bound of the differential stress, which is twice the maximum shear stress. The average differential stress was estimated to be at least 20 MPa over the entire region with peaks of 62 MPa. The minimum differential stress in the Landers area, specifically, was estimated to be 20–30 MPa at seismogenic depth. This value was equivalent to the maximum shear stress of 10–15 MPa, which is the value that is the most consistent with the absolute stress field with $C = 0.5$ presented in this study. When investigating the temporal change in shear stresses acting on the main shock faults and those in the elastic strain energy caused by the Landers earthquake, the estimate is barely significant (Figure 7b). However, based on the coseismic stress rotation, it seems too low (Figure 6b).

Hardebeck and Hauksson (2001) estimated the maximum shear stress on the main shock faults of the Landers earthquake to be 12 MPa with an upper limit of 25–32 MPa. They simplified the absolute stress field via a 2-D uniform stress tensor and assumed an average stress drop of 8 MPa. Next, they constrained the maximum shear stress, based on the observed rotation of the maximum principal stress axes. This value is equivalent to 27%–71% of the estimate at a depth of 5 km in our study. The maximum shear stresses of the coseismic stress perturbation due to the Landers earthquake were 17 and 9 MPa on average within 1 km from the main shock fault at depths of 5 and 10 km, respectively (Figures 5 and S3). If Hardebeck and Hauksson (2001) had used the same stress drop as the average stress drop calculated in the present study (13 MPa at depths of 5–10 km), the maximum shear stress would have been estimated to be 20 MPa with an upper limit of 41–52 MPa. The average value of this rough estimate was still smaller than the best estimate of the present study (62 ± 19 MPa at depths of 5–10 km), but both were consistent within the estimation errors.

The frictional strength of the SAF is of great interest. The SAF bends about 20° at the *Big Bend* in the Transverse Ranges of southern California (Figure 2). This bend causes a collision at the Mojave segment (MJS) of the SAF. Because the strike of the MJS is oblique to the direction of the relative plate motion between the Pacific and North American plates, this causes fault-normal stresses due to plate convergence and shear stresses resulting from frictional resistance at the MJS. Since the system of the SAF consists of transcurrent plate boundaries, fault-normal stresses must be inevitably accommodated by thrust faulting with a strike

parallel to the MJS in the adjacent crust (Scholz, 2000). The ratio of the shear stress to the fault-normal stress changes spatially with distance from the MJS, which characterizes the stress pattern across the MJS. By combining the 3-D numerical simulation of tectonic loading and stress inversion (Terakawa & Matsu'ura, 2008), Terakawa and Matsu'ura (2009) determined the effective friction coefficient μ' of the MJS to be 0.3 and the frictional strength to be 140 MPa at a depth of 6 km. In this numerical simulation, the friction coefficient of the adjacent thrust faults was assumed to be 0.6 under dry conditions. If Terakawa and Matsu'ura (2009) had assumed a hydrostatic condition for the thrust faults, the frictional strength of the MJS at a depth of 5 km would have been 82 MPa.

The source region of the Landers earthquake is located near the southernmost end of the MJS, where the strike of the SAF is almost parallel to the direction of relative plate motion (Figure 2). Therefore, we can rationally assume the normal stress on the pure transcurrent segment to be lithostatic. If the effective friction coefficient μ' is assumed to be the same as that of the MJS (0.3) estimated by Terakawa and Matsu'ura (2009), the frictional strength of the SAF adjacent to the source region of the Landers earthquake would be estimated to be about 36 MPa at a depth of 5 km, with rock densities of 3,000 kg/m^3. The excess pore pressure above hydrostatic was simultaneously estimated to be 14 MPa (C = 0.25). The frictional strength is about twice as large as the upper limit of that inferred from heat flow data obtained using conductive process of frictional heating (Brune et al., 1969; Lachenbruch & Sass, 1980). Recent numerical simulation of conductive process coupled with fluid flow (Fulton et al., 2004; Saffer et al., 2003) tends to estimate lower strengths (10 MPa) than the simple convection models. Nevertheless, the rough estimate of the frictional strength of 36 MPa is on the same order, and not inconsistent with the estimates from heat flow data, within the measurement errors.

The source region of the Landers earthquake is 20–30 km to the north of the SAF (Figure 2). The rough estimate of the frictional strength of the SAF adjacent to the source region (36 MPa) was equivalent to 80% of the average maximum shear stress in southern California (44 ± 15 MPa). When calculating absolute stress tensors from the focal mechanisms in section 3.2, we used uniform overpressure coefficients of reference pore pressures for all the events and did not distinguish between events occurring at the SAF and other intraplate events. Therefore, the maximum shear stress at and around the SAF may have been overestimated (Figure 4).

Once the current absolute stress fields are estimated, one can monitor the stress state together with the estimation errors in real time by evaluating stress perturbations from seismic/geodetic data. The information provided in this study will enable traditional analyses of the stress transfer (King et al., 1994; Meier et al., 2014; Stein, 1999; Terakawa et al., 2013) to be more powerful in evaluating aftershock sequences in a short-term period ($<10^0$ year) following large/huge earthquakes. To monitor the stress state over the medium term (decades), effects of viscoelastic behavior in the asthenosphere should be incorporated into the method of estimating the absolute stress fields presented in this study. To understand the generation of major earthquakes over the long term ($>10^2$ years), it is further necessary to consider and incorporate the effects of tectonic loading at plate boundaries into the method. However, it is more difficult to monitor the frictional strength of active faults/plate boundaries, because pore fluid pressures may change in space and time more rapidly than the loading process (Bosl & Nur, 2002; Miller et al., 2004; Nur & Booker, 1972; Terakawa, 2014). Knowledge of both stress and crustal strength will contribute to disaster mitigation.

5. Conclusions

In the present study, we proposed a method to model the 3-D absolute stress field using earthquake focal mechanisms and the reference pore pressure as a single parameter. In the method, the six components of the absolute stress tensors were calculated by examining the fault orientations relative to the stress pattern and by assuming the Coulomb failure criterion characterized by the reference pore pressure. An inversion scheme based on Bayesian statistical inference and ABIC was then applied to the data set of absolute stress tensors in order to model the 3-D absolute stress field. Loading processes were not assumed in this method. The 3-D absolute stress field was modeled from thousands of focal mechanisms in southern California. Furthermore, the coseismic stress perturbation caused by the main shock was calculated, which revealed the quantitative relationship between the coseismic stress rotation and the reference pore pressure. With constraints on the coseismic stress rotation obtained through the stress inversion analysis, temporal changes in the shear stress acting on the main shock faults, and those in the elastic strain energy, the most appropriate reference pore pressures required to estimate the 3-D absolute stress field in the source region of the Landers

earthquake were determined. The maximum shear stresses immediately before the Landers earthquake were at least 44 ± 15 and 79 ± 24 MPa at depths of 5 and 10 km, respectively, under the hydrostatic reference pore pressure. We conclude that the state of stress on inland active faults, including the main shock faults of the Landers earthquake, is appropriately described by the Anderson-Byerlee stress condition.

Acknowledgments
We are highly grateful to the two anonymous reviewers for their useful suggestions. We would like to thank the Editor Martha Savage. We would like to thank the Southern California Earthquake Data Center (doi:10.7909/C3WD3xH1) for providing focal mechanism solutions in the Southern California Seismic Network catalog (doi:10.7914/SN/CI). This work was supported by a Grant-in Aid for Scientific Research C (26400451). The data that support the findings of this study are available at https://service.scedc.caltech.edu/eq-catalogs/FMsearch.php.

References

Akaike, H. (Ed.) (1977). *On entropy maximization principle* (pp. 27–41). Amsterdam: North-Holland.
Akaike, H. (Ed.) (1980). *Likelihood and Bayes procedure* (pp. 143–166). Valencia: University Press.
Anderson, E. M. (1951). *The dynamics of faulting and dyke formation with applications to Britain* (2nd ed., p. 206). London: Oliver.
Bird, P. (2003). An updated digital model of plate boundaries. *Geochemistry, Geophysics, Geosystems*, *4*(3), 1027. https://doi.org/10.1029/2001GC000252
Bird, P. (2017). Stress field models from Maxwell stress functions: Southern California. *Geophysical Journal International*, *210*(2), 951–963. https://doi.org/10.1093/gji/ggx207
Bosl, W. J., & Nur, A. (2002). Aftershocks and pore fluid diffusion following the 1992 Landers earthquake. *Journal of Geophysical Research*, *107*(B12), 2366. https://doi.org/10.1029/2001JB000155
Brudy, M., Zoback, M. D., Fuchs, K., Rummel, F., & Baumgartner, J. (1997). Estimation of the complete stress tensor to 8 km depth in the KTB scientific drill holes: Implications for crustal strength. *Journal of Geophysical Research*, *102*(B8), 18,453–18,475. https://doi.org/10.1029/96JB02942
Brune, J. N., Henyey, T. L., & Roy, R. F. (1969). Heat flow, stress, and rate of slip along San Andreas Fault, California. *Journal of Geophysical Research*, *74*(15), 3821–3827. https://doi.org/10.1029/JB074i015p03821
Byerlee, J. (1978). Friction of rocks. *Pure and Applied Geophysics*, *116*(4–5), 615–626. https://doi.org/10.1007/BF00876528
Fukahata, Y., & Matsu'ura, M. (2005). General expressions for internal deformation fields due to a dislocation source in a multilayered elastic half-space. *Geophysical Journal International*, *161*(2), 507–521. https://doi.org/10.1111/j.1365-246X.2005.02594.x
Fukahata, Y., & Matsu'ura, M. (2006). Quasi-static internal deformation due to a dislocation source in a multilayered elastic/viscoelastic half-space and an equivalence theorem. *Geophysical Journal International*, *166*(1), 418–434. https://doi.org/10.1111/j.1365-246X.2006.02921.x
Fulton, P. M., Saffer, D. M., Harris, R. N., & Bekins, B. A. (2004). Re-evaluation of heat flow data near Parkfield, CA: Evidence for a weak San Andreas Fault. *Geophysical Research Letters*, *31*, L15S15. https://doi.org/10.1029/2003GL019378
Gephart, J. W., & Forsyth, D. W. (1984). An improved method for determining the regional stress tensor using earthquake focal mechanism data—Application to the San-Fernando earthquake sequence. *Journal of Geophysical Research*, *89*(B11), 9305–9320. https://doi.org/10.1029/JB089iB11p09305
Hanks, T. C., & Kanamori, H. (1979). A moment magnitude scale. *Journal of Geophysical Research*, *84*(B5), 2348–2350.
Hardebeck, J. L., & Hauksson, E. (2001). Crustal stress field in southern California and its implications for fault mechanics. *Journal of Geophysical Research*, *106*(B10), 21,859–21,882. https://doi.org/10.1029/2001JB000292
Hardebeck, J. L., & Michael, A. J. (2006). Damped regional-scale stress inversions: Methodology and examples for southern California and the Coalinga aftershock sequence. *Journal of Geophysical Research*, *111*, B11310. https://doi.org/10.1029/2005JB004144
Häring, M. O., Schanz, U., Ladner, F., & Dyer, B. C. (2008). Characterisation of the Basel 1 enhanced geothermal system. *Geothermics*, *37*(5), 469–495. https://doi.org/10.1016/j.geothermics.2008.06.002
Hasegawa, A., Yoshida, K., & Okada, T. (2011). Nearly complete stress drop in the 2011 M_w 9.0 off the Pacific coast of Tohoku earthquake. *Earth, Planets and Space*, *63*(7), 703–707. https://doi.org/10.5047/eps.2011.06.007
Hauksson, E., Jones, L. M., Hutton, K., & Eberhartphillips, D. (1993). The 1992 Landers earthquake sequence—Seismological observations. *Journal of Geophysical Research*, *98*(B11), 19,835–19,858. https://doi.org/10.1029/93JB02384
Heidbach, O., Tingay, M., Barth, A., Reinecker, J., Kurfeß, D., & Müller, B. (2008). The World Stress Map database release 2008. Retrieved from http://www.world-stress-map.org/, last accessed 27 November 2017, https://doi.org/10.1594/GFZ.WSM.Rel2008
Horiuchi, S., Rocco, G., & Hasegawa, A. (1995). Discrimination of fault planes from auxiliary planes based on simultaneous determination of stress tensor and a large number of fault plane solutions. *Journal of Geophysical Research*, *100*(B5), 8327–8338. https://doi.org/10.1029/94JB03284
Jackson, D. D., & Matsuura, M. (1985). A Bayesian-approach to nonlinear inversion. *Journal of Geophysical Research*, *90*(NB1), 581–591. https://doi.org/10.1029/JB090iB01p00581
Jennings, C. W. (1994). Fault activity map of California and adjacent areas, with locations and ages of recent volcanic eruptions, *Calif. Div. Mines and Geology*, Geologic Data Map No. 6, map scale 1:750,000.
Kanamori, H., Mori, J., Hauksson, E., Heaton, T. H., Hutton, L. K., & Jones, L. M. (1993). Determination of earthquake energy-release and M_L using TERRASCOPE. *Bulletin of the Seismological Society of America*, *83*(2), 330–346.
King, G. C. P., Stein, R. S., & Lin, J. (1994). Static stress changes and the triggering of earthquakes. *Bulletin of the Seismological Society of America*, *84*(3), 935–953.
Lachenbruch, A. H., & Sass, J. H. (1980). Heat-flow and energetics of the San-Andreas fault zone. *Journal of Geophysical Research*, *85*(NB11), 6185–6222. https://doi.org/10.1029/JB085iB11p06185
Lockner, D. A., Morrow, C., Moore, D., & Hickman, S. (2011). Low strength of deep San Andreas fault gouge from SAFOD core. *Nature*, *472*(7341), 82–85. https://doi.org/10.1038/nature09927
Luttrell, K., & Sandwell, D. (2012). Constraints on 3-D stress in the crust from support of mid-ocean ridge topography. *Journal of Geophysical Research*, *117*, B04402. https://doi.org/10.1029/2011JB008765
Luttrell, K., & Smith-Konter, B. (2017). Limits on crustal differential stress in southern California from topography and earthquake focal mechanisms. *Geophysical Journal International*, *211*(1), 472–482. https://doi.org/10.1093/gji/ggx301
Luttrell, K. M., Tong, X. P., Sandwell, D. T., Brooks, B. A., & Bevis, M. G. (2011). Estimates of stress drop and crustal tectonic stress from the 27 February 2010 Maule, Chile, earthquake: Implications for fault strength. *Journal of Geophysical Research*, *116*, B11401. https://doi.org/10.1029/2011JB008509
McKenzie, D. P. (1969). The relation between fault plane solutions for earthquakes and directions of principal stresses. *Bulletin of the Seismological Society of America*, *59*(2), 591–601.
Meier, M. A., Werner, M. J., Woessner, J., & Wiemer, S. (2014). A search for evidence of secondary static stress triggering during the 1992 M_w 7.3 Landers, California, earthquake sequence. *Journal of Geophysical Research: Solid Earth*, *119*, 3354–3370. https://doi.org/10.1002/2013JB010385

Michael, A. J. (1984). Determination of stress from slip data—Faults and folds. *Journal of Geophysical Research*, *89*(NB13), 1517–1526.
Michael, A. J. (1987). Use of focal mechanisms to determine stress—A control study. *Journal of Geophysical Research*, *92*(B1), 357–368. https://doi.org/10.1029/JB092iB01p00357
Miller, S. A., Collettini, C., Chiaraluce, L., Cocco, M., Barchi, M., & Kaus, B. J. P. (2004). Aftershocks driven by a high-pressure CO_2 source at depth. *Nature*, *427*(6976), 724–727. https://doi.org/10.1038/nature02251
Noda, H., & Lapusta, N. (2010). Three-dimensional earthquake sequence simulations with evolving temperature and pore pressure due to shear heating: Effect of heterogeneous hydraulic diffusivity. *Journal of Geophysical Research*, *115*, B12314. https://doi.org/10.1029/2010JB007780
Nur, A., & Booker, J. R. (1972). Aftershocks caused by pore fluid-flow. *Science*, *175*(4024), 885–887. https://doi.org/10.1126/science.175.4024.885
Rice, J. R. (1992). Fault stress states, pore pressure distributions, and the weakness of the San Andreas Fault. In *Fault mechanics and transport properties of rocks* (pp. 475–503). San Diego, CA: Academic Press.
Rice, J. R. (2006). Heating and weakening of faults during earthquake slip. *Journal of Geophysical Research*, *111*, B05311. https://doi.org/10.1029/2005JB004006
Rivera, L., & Cisternas, A. (1990). Stress tensor and fault plane solutions for a population of earthquakes. *Bulletin of the Seismological Society of America*, *80*(3), 600–614.
Saffer, D. M., Bekins, B. A., & Hickman, S. (2003). Topographically driven groundwater flow and the San Andreas heat flow paradox revisited. *Journal of Geophysical Research*, *108*(B5), 2274. https://doi.org/10.1029/2002JB001849
Scholz, C. H. (2000). Evidence for a strong San Andreas Fault. *Geology*, *28*(2), 163–166. https://doi.org/10.1130/0091-7613(2000)028<0163:efassa>2.3.co;2
Sibson, R. H. (1992). Implications of fault-valve behavior for rupture nucleation and recurrence. *Tectonophysics*, *211*(1–4), 283–293. https://doi.org/10.1016/0040-1951(92)90065-e
Stein, R. S. (1999). The role of stress transfer in earthquake occurrence. *Nature*, *402*(6762), 605–609. https://doi.org/10.1038/45144
Terakawa, T. (2014). Evolution of pore fluid pressures in a stimulated geothermal reservoir inferred from earthquake focal mechanisms. *Geophysical Research Letters*, *41*, 7468–7476. https://doi.org/10.1002/2014GL061908
Terakawa, T. (2017). Overpressurized fluids drive microseismic swarm activity around Mt. Ontake volcano, Japan. *Earth, Planets and Space*, *69*(1), 1–10. https://doi.org/10.1186/s40623-017-0671-x
Terakawa, T., Hashimoto, C., & Matsu'ura, M. (2013). Changes in seismic activity following the 2011 Tohoku-oki earthquake: Effects of pore fluid pressure. *Earth and Planetary Science Letters*, *365*, 17–24. https://doi.org/10.1016/j.epsl.2013.01.017
Terakawa, T., & Matsu'ura, M. (2008). CMT data inversion using a Bayesian information criterion to estimate seismogenic stress fields. *Geophysical Journal International*, *172*(2), 674–685. https://doi.org/10.1111/j.1365-246X.2007.03656.x
Terakawa, T., & Matsu'ura, M. (2009). Strength of the San Andreas Fault inferred from tectonic loading simulation and CMT data inversion. *Geophysical Journal International*, *178*(3), 1663–1676. https://doi.org/10.1111/j.1365-246X.2009.04207.x
Terakawa, T., Miller, S. A., & Deichmann, N. (2012). High fluid pressure and triggered earthquakes in the enhanced geothermal system in Basel, Switzerland. *Journal of Geophysical Research*, *117*, B07305. https://doi.org/10.1029/2011JB008980
Terakawa, T., Zoporowski, A., Galvan, B., & Miller, S. A. (2010). High-pressure fluid at hypocentral depths in the L'Aquila region inferred from earthquake focal mechanisms. *Geology*, *38*(11), 995–998. https://doi.org/10.1130/g31457.1
Trugman, D. T., & Shearer, P. M. (2017). Application of an improved spectral decomposition method to examine earthquake source scaling in Southern California. *Journal of Geophysical Research: Solid Earth*, *122*, 2890–2910. https://doi.org/10.1002/2017JB013971
Wald, D. J., & Heaton, T. H. (1994). Spatial and temporal distribution of slip for the 1992 Landers, California, earthquake. *Bulletin of the Seismological Society of America*, *84*(3), 668–691.
Wesson, R. L., & Boyd, O. S. (2007). Stress before and after the 2002 Denali fault earthquake. *Geophysical Research Letters*, *34*, L07303. https://doi.org/10.1029/2007GL029189
Yabuki, T., & Matsu'ura, M. (1992). Geodetic data inversion using a Bayesian information criterion for spatial-distribution of fault slip. *Geophysical Journal International*, *109*(2), 363–375. https://doi.org/10.1111/j.1365-246X.1992.tb00102.x
Yamashita, F., Fukuyama, E., & Omura, C. (2004). Estimation of fault strength: Reconstruction of stress before the 1995 Kobe earthquake. *Science*, *306*(5694), 261–263. https://doi.org/10.1126/science.1101771
Yang, W. Z., & Hauksson, E. (2013). The tectonic crustal stress field and style of faulting along the Pacific North America Plate boundary in Southern California. *Geophysical Journal International*, *194*(1), 100–117. https://doi.org/10.1093/gji/ggt113
Yang, W. Z., Hauksson, E., & Shearer, P. M. (2012). Computing a large refined catalog of focal mechanisms for Southern California (1981-2010): Temporal stability of the style of faulting. *Bulletin of the Seismological Society of America*, *102*(3), 1179–1194. https://doi.org/10.1785/0120110311
Zoback, M. D., & Healy, J. H. (1992). In situ stress measurements to 3.5 km depth in the Cajon pass scientific-research borehole—Implications for the mechanics of crustal faulting. *Journal of Geophysical Research*, *97*(B4), 5039–5057. https://doi.org/10.1029/91JB02175
Zoback, M. D., & Townend, J. (2001). Implications of hydrostatic pore pressures and high crustal strength for the deformation of intraplate lithosphere. *Tectonophysics*, *336*(1–4), 19–30. https://doi.org/10.1016/s0040-1951(01)00091-9
Zoback, M. D., Zoback, M. L., Mount, V. S., Suppe, J., Eaton, J. P., Healy, J. H., et al. (1987). New evidence on the state of stress of the San-Andreas fault system. *Science*, *238*(4830), 1105–1111. https://doi.org/10.1126/science.238.4830.1105